Multi-physics modeling of non-isothermal compositional flow on adaptive grids

Benjamin Faigle [a,*], Mohamed Ahmed Elfeel [b], Rainer Helmig [a], Beatrix Becker [a], Bernd Flemisch [a], Sebastian Geiger [b]

[a] *IWS, Department of Hydromechanics and Modelling of Hydrosystems, University of Stuttgart, Germany*
[b] *Institute of Petroleum Engineering, Heriot-Watt University, Edinburgh, United Kingdom*

Abstract

A multi-physics framework for compositional and non-isothermal two-phase flow in a porous medium is presented which adapts locally the model complexity depending on the physical state. It is based on a sequential (IMPET) solution scheme. As a second adaptive strategy, the simulation grid can be refined locally. This may lead to a mesh with hanging nodes, which is treated by a multi-point flux approximation (MPFA) for improved flux representation. The two adaptivity concepts are employed to simulate a combined subsurface CO_2 injection and geothermal application in an existing reservoir, the Tensleep formation.
© 2014 Published by Elsevier B.V.

1. Introduction

Numerical models for subsurface flow and transport often have to cover long time periods and large spatial domains. If, for example, CO_2 is to be injected into the subsurface to mitigate its effect as a greenhouse gas, it is of interest whether the CO_2 could leak back in the atmosphere or whether the displaced brine might encroach upon valuable freshwater resources. In such a case, the simulation domain has to cover more than only the vicinity of the injection well, and the simulation tool needs to be able to mimic the relevant physical processes. Such detailed modeling on field scales requires the development of efficient modeling tools.

In this example and also in many other interesting applications of multi-phase flow in porous media, the local level of complexity is highly variable. Complex flow regimes that need to be resolved in great detail may occur only in

---
* Corresponding author.
E-mail addresses: benjamin.faigle@iws.uni-stuttgart.de (B. Faigle), mohamed.ahmed@pet.hw.ac.uk (M.A. Elfeel), rainer.helmig@iws.uni-stuttgart.de (R. Helmig), beatrix.becker@iws.uni-stuttgart.de (B. Becker), bernd.flemisch@iws.uni-stuttgart.de (B. Flemisch), sebastian.geiger@pet.hw.ac.uk (S. Geiger).

ARTICLE IN PRESS

2   *B. Faigle et al. / Comput. Methods Appl. Mech. Engrg. ▮ (▮▮▮▮) ▮▮▮–▮▮▮*
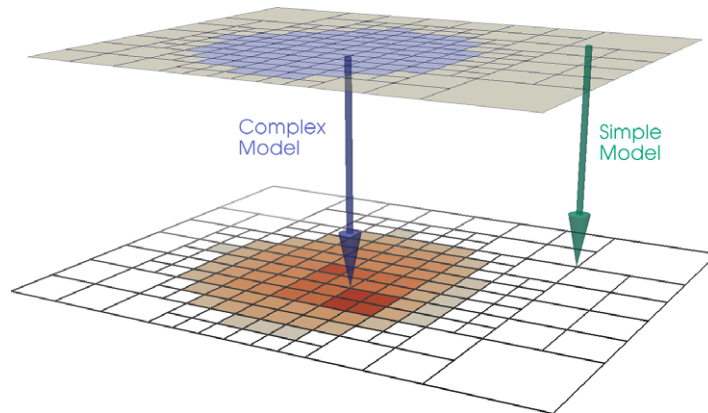
Fig. 1. Schematic of the multi-physics framework: different models are applied locally to model the combined problem. The simulation grid is adaptively refined around the red plume to capture the complex physical processes occurring here. (For interpretation of the references to color in this figure legend, the reader is referred to the web version of this article.)

a small region of the whole modeling domain, which means that a fine grid is required only in that region while a coarse grid might be sufficient in the rest of the domain. Likewise, the physical processes may require a more detailed conceptual approximation of the model locally, while a simpler conceptual model might be sufficient in other model regions. Over long periods of time, some driving forces may become more significant and others less. At best, the level of numerical detail should be adapted to the underlying processes and not be decided a priori by the modeler.

The multi-physics concept adapts the complexity of the numerical model locally according to the underlying physical processes. Complicated physics are approached with complex abstractions that differ from those applied in flow regimes that remain simple (Fig. 1). More specifically, a model with a simplified treatment of non-isothermal behavior is used if the temperature variation is sufficiently small, and two-phase conditions are only considered in simulation cells if more than a single phase can be present. The regions in which a particular model is applied need to be updated in each time steps, requiring the development of corresponding indicators for the allocation of each model. In addition to the model adaptivity, an adaptive refinement of the computational grid gains detail and accuracy in regions of interest while the global system remains coarse enough to be solved with reasonable effort. These dynamic or adaptive simulation frameworks attempt to find a balance between accuracy and detail, reason and efficiency. They allow us to use locally the appropriate and best numerical method and grid resolution available.

In the remainder of this introduction, our developments are put in the appropriate literature context. Section 2 presents the full numerical model for non-isothermal compositional two-phase flow including a multi-point flux approximation that is applicable to adaptive grids with hanging nodes. In Section 3, a multi-physics concept is introduced that divides the computational domain in four possibly time-dependent sub-domains according to the underlying local physical processes. Section 4 first provides a simple example that illustrates the efficiency gain for using this multi-physics model compared to the full model, and then presents an application to a realistic field-case scenario. Finally, some conclusions are given in 5.

1.1. Literature context

This study employs the numerical models for compositional two-phase flow and the multi-physics framework to combine individual models of different complexity that were developed in [1,2]. The bonding of the models is simplified by formulating them mathematically by means of one pressure equation based on [3] and sequentially solved transport equations; this circumvents coupling by domain decomposition techniques [4,5] because the mathematical structure of the equations and number of primary variables remains the same for all models. Decomposition techniques, however, would also allow the use of different numerical solution schemes for the individual models [6]. A good overview of different coupling schemes and multi-physics models can be found in Wheeler and Peszyńska [7].

The second branch of adaptivity considered here involves a dynamic adjustment of the simulation grid, with focus on regular grids. Adaptive mesh refinement increases the resolution of the simulation mesh in regions of high interest

ARTICLE IN PRESS

B. Faigle et al. / Comput. Methods Appl. Mech. Engrg. ▮ (▮▮▮▮) ▮▮▮–▮▮▮

3

while maintaining a coarse grid everywhere else. The technique is widely used in research into porous media flow and is being developed further [8–10]; many authors nest the refined areas in the coarse grid in a multi-grid or domain decomposition framework [11–16], allowing for parallel computations and an individual temporal resolution of patches of coarse and fine grid. In the former approach on an integrated adaptive grid, the flux stencil has to be increased locally to avoid erroneous fluxes over interfaces between fine to coarse cells. A class of methods capable of doing this, the so-called Multi-Point Flux Approximation (MPFA), was initiated by [17,18]. One particular MPFA, the L-method [19,20], is perfectly suited for irregular grids that develop if regular grids are refined or coarsened.

2. Model for non-isothermal compositional two-phase flow

In the following, the full numerical model for the simulation of non-isothermal compositional two-phase flow is presented. Section 2.1 presents the mathematical model that consists of one mass balance for each component and one energy balance. The time discretization in form of a sequential solution scheme is provided in Section 2.2. Particular emphasis if paid to the calculation of the appropriate time step size in Section 2.3, where a new way of incorporating the conduction term is given. Section 2.4 presents the spatial discretization in form of a multi-point flux approximation method that allows hanging nodes on adaptively refined grids. The required flash calculations are explained in Section 2.5.

2.1. Mathematical model

The conservation of mass valid for compositional two-phase flow in porous media can be formulated for each component κ in the phases α as

$$\sum_\alpha \frac{\partial(\phi S_\alpha \varrho_\alpha X_\alpha^\kappa)}{\partial t} + \nabla \cdot \left(\sum_\alpha X_\alpha^\kappa \varrho_\alpha \mathbf{v}_\alpha + \mathbf{J}_\alpha^\kappa\right) + q^\kappa = 0. \tag{1}$$

We denote the porosity ϕ, S_α is the phase saturation, t represents the time, and q^κ are sources or sinks. Supplementary thermodynamic constraints specify the density ϱ_α and the solubility limits to calculate mass fractions X_α^κ. The details of the thermodynamic relations used in this study can be found in [21]. The diffusive flux $\mathbf{J}$ plays a minor role for the length scales considered here and will thus be neglected in the following. We express the phase velocity $\mathbf{v}_\alpha$ by

$$\mathbf{v}_\alpha = -\lambda_\alpha \mathbf{K}(\nabla p_\alpha - \varrho_\alpha \mathbf{g}), \tag{2}$$

where λ_α is the phase mobility, $\mathbf{K}$ the intrinsic permeability of the porous medium, and $\mathbf{g}$ the gravity vector. The phase pressures p_α are related via a macro-scale capillary pressure–saturation relationship $p_c(S)$ in the parameterization of BROOKS–COREY

$$p_c(S_w) = p_d \left(\frac{S_w - S_{wr}}{1 - S_{wr}}\right)^{-\frac{1}{\lambda}} \quad \text{for } p_c \geq p_d. \tag{3}$$

On the assumption of local thermodynamic equilibrium, energy is conserved if

$$\frac{\partial\left(\phi \sum_\alpha S_\alpha \varrho_\alpha u_\alpha + (1-\phi)\varrho_s c_s T\right)}{\partial t} + \nabla \cdot \left(\sum_\alpha (h_\alpha \varrho_\alpha \mathbf{v}_\alpha - \bar{\lambda}_E \nabla T)\right) + q^E = 0. \tag{4}$$

The storage term in the energy balance comprises both the energy stored in all fluids, where u_α expresses the mass-specific internal energy of phase α, as well as the energy of the solid phase by means of its heat capacity c_s. The temperature is denoted T, and the phase enthalpy h_α. It is again noted that diffusive fluxes are neglected. Therefore, thermal convection comprises the heat transport through advective fluxes, supplemented by the conductive heat flux of the porous medium. Conduction is expressed in terms of the combined heat conductivity $\bar{\lambda}_E$ of the fluids and the porous medium.

ARTICLE IN PRESS

4 *B. Faigle et al. / Comput. Methods Appl. Mech. Engrg. ▮ (▮▮▮▮) ▮▮▮–▮▮▮*

2.2. Time discretization

We employ an "IMPET" (Implicit Pressure, Explicit Transport) scheme, where the conservation equations of the last section are reformulated into one pressure equation to obtain a flow field for the transport equations. This specific approach was proposed by [3] and analyzed in [22,23]. We follow the derivation in [24].

Porosity is defined as the void space in the porous media that can be accessed by and is filled by a specific volume of fluids, $\hat{v} = \sum_\alpha v_\alpha$ (m^3/m^3), which yields

$$\hat{v} = \phi. \tag{5}$$

We now approximate the changes in time by a Taylor series. On the assumption of a rigid porous medium, the right hand side of the volume balance remains unchanged,

$$\hat{v}(t) + \Delta t \frac{\partial \hat{v}}{\partial t} + \mathcal{O}\left(\Delta t^2\right) = \phi. \tag{6}$$

Under non-isothermal conditions, the fluid volume changes in time if there are variations of pressure, a change of mass or of energy,

$$\frac{\partial \hat{v}}{\partial t} = \frac{\partial \hat{v}}{\partial p}\frac{\partial p}{\partial t} + \sum_\kappa \frac{\partial \hat{v}}{\partial C^\kappa}\frac{\partial C^\kappa}{\partial t} + \frac{\partial \hat{v}}{\partial \hat{u}}\frac{\partial \hat{u}}{\partial t}, \tag{7}$$

where $C^\kappa = \phi \sum_\alpha \varrho_\alpha S_\alpha X_\alpha^\kappa$ represents the total concentration, which accounts for the total mass of a component in a specific volume, so it is not a phase density.

Inserting (7) in (6), neglecting the higher-order terms, and reordering yields

$$\frac{\partial \hat{v}}{\partial p}\frac{\partial p}{\partial t} + \sum_\kappa \frac{\partial \hat{v}}{\partial C^\kappa}\frac{\partial C^\kappa}{\partial t} + \frac{\partial \hat{v}}{\partial \hat{u}}\frac{\partial \hat{u}}{\partial t} = \frac{\phi - \hat{v}}{\Delta t}. \tag{8}$$

The first term in this pressure equation accounts for changes in the fluid volume caused by variations in pressure. It can be rewritten in terms of the total compressibility $\hat{c} = \partial \hat{v}/\partial p$ of the fluid mixture. The second summand expresses the variation of total fluid volume with a change of mass (for details, see [25]). It contains a partial derivative of fluid volume over mass, $\partial \hat{v}/\partial C^\kappa = \partial \hat{v}/\partial m^\kappa$, multiplied by the local changes in mass due to fluxes through the cell interfaces, $\partial C^\kappa/\partial t$. These changes in mass are quantified by the traditional transport equation for the components, derived from mass conservation (see [25]),

$$\frac{\partial C^\kappa}{\partial t} = -\nabla \cdot \left(\sum_\alpha \varrho_\alpha \mathbf{v}_\alpha X_\alpha^\kappa\right) - q^\kappa. \tag{9}$$

The successive term captures the feedback from changes of the total internal energy $\hat{u} = \phi \sum_\alpha S_\alpha \varrho_\alpha u_\alpha + (1 - \phi)\varrho_s c_s T$, which is accordingly given by the transport equation for energy,

$$\frac{\partial \hat{u}}{\partial t} = -\nabla \cdot \left(\sum_\alpha h_\alpha \varrho_\alpha \mathbf{v}_\alpha - \bar{\lambda}_E \nabla T\right) - q^E. \tag{10}$$

The term on the right-hand side of (8) vanishes if the volume constraint in (5) is fulfilled. However, if the fluids involved are partially miscible and compressible and the changes in fluid density are not implicitly incorporated, a residual $\epsilon = \frac{\phi - \hat{v}}{\Delta t}$ remains which will be discussed in more detail in Section 2.4.

2.3. Time-step constraint

The explicit treatment in the transport step restricts the size of the time-step [26],

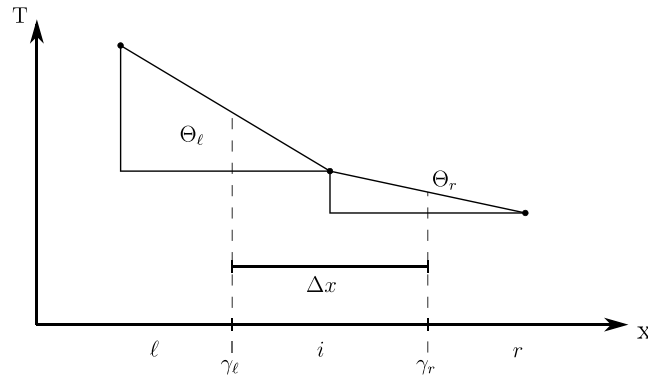$$\Delta t = a\left(\frac{S_i}{F_i}\right), \quad a \leq 1. \tag{11}$$

ARTICLE IN PRESS

B. Faigle et al. / Comput. Methods Appl. Mech. Engrg. ▮ (▮▮▮▮) ▮▮▮–▮▮▮   5

Fig. 2. Schematic one-dimensional description of the time-step limitation for the conduction term.

This *CFL*-like criterion requires that the representative flux F_i may not exceed the available storage S_i, which needs to be valid for all conservation equations, for mass and energy. For the transport of mass, we employ $S_i = \sum_\kappa C^\kappa$, and the maximum of the observed out- or in-flux of cell i as proposed in [27],

$$F_i = \max_{\gamma \in \mathcal{N}_i} \sum_\alpha \left| \mathbf{n}_\gamma^T \mathbf{v}_{\alpha,\gamma} A_\gamma \right|. \tag{12}$$

Above, $\mathcal{N}_i$ denotes the set of interfaces of cell i to neighboring cells, γ one such interface with area A_γ, $\mathbf{n}_\gamma$ the normal vector pointing outward of i and $\mathbf{v}_{\alpha,\gamma}$ the α-phase velocity associated with γ.

We now proceed with the derivation of an appropriate *CFL*-like criterion for the transport of energy and will define quantities S_i^E and F_i^E corresponding to (11). Wherever no ambiguity arises, the subscripts i and γ are dropped for the sake of brevity. For thermal systems, Geiger et al. [28] propose a criterion derived from the linearized form of (10) with respect to temperature,

$$\hat{c}_p \frac{\partial T}{\partial t} = -\nabla \cdot \left(\sum_\alpha c_{p,\alpha} \varrho_\alpha \mathbf{v}_\alpha T - \bar{\lambda}_E \nabla T \right) - q^E, \tag{13}$$

where $\hat{c}_p = (1 - \phi)\varrho_s c_{p,s} + \phi \sum_\alpha \varrho_\alpha c_{p,\alpha} S_\alpha$ abbreviates the combined heat capacity of all fluids and the solid. This equation can be reformulated in terms of S^E and F^E of (11), if internal sources of energy and conduction are neglected, and by dropping the mixed term $-T\nabla \cdot F^E$, yielding

$$S^E \frac{\partial T}{\partial t} = -F^E \nabla \cdot T. \tag{14}$$

It provides the energy equivalent of the storage $S_i^E = V_i \hat{c}_p$. Geiger et al. [28] relate the energy flux function F^E to a "heat transfer velocity" $\mathbf{v}_{th}$,

$$\mathbf{v}_{th} := \frac{\sum_\alpha c_{p,\alpha} \varrho_\alpha \mathbf{v}_\alpha}{\hat{c}_p}. \tag{15}$$

The conduction term in (13), however, can only be cast into the form of (14), if the temperature T can be factored out of the gradient ∇T in (13). This can be achieved by defining a specific interpolation of ∇T that is described in the following for one dimension and uniform grid spacing.

Given a regular grid, cell i lies between its neighbors ℓ and r (Fig. 2). The normal components of the temperature gradients at both interfaces γ_ℓ and γ_r are given by

$$\Theta_\ell = \mathbf{n}_{\gamma_\ell}^T \nabla T(\gamma_\ell) = \frac{T_\ell - T_i}{\Delta x}, \tag{16}$$

$$\Theta_r = \mathbf{n}_{\gamma_r}^T \nabla T(\gamma_r) = \frac{T_r - T_i}{\Delta x}. \tag{17}$$

ARTICLE IN PRESS

6   B. Faigle et al. / Comput. Methods Appl. Mech. Engrg. ∎ (∎∎∎∎) ∎∎∎–∎∎∎

Let $\Theta(x)$ be the interpolation function for the gradient ∇T that satisfies

$$\frac{\partial \Theta(x)}{\partial x} = \xi \, \Theta(x), \tag{18}$$

for a constant value of ξ on cell i, i.e. $x \in (\gamma_\ell, \gamma_r)$. The requirement (18) allows us to factor out the temperature T in (13) if the value of ξ can be determined by the discrete values Θ_ℓ and Θ_r at the boundary of cell i. From (17) and (18), it follows that

$$\Theta(x) = \Theta_r e^{\xi(x-\gamma_r)}. \tag{19}$$

Inserting (16) for x at the position of γ_ℓ gives

$$e^{\xi(\Delta x)} = \frac{\Theta_\ell}{\Theta_r}, \tag{20}$$

with $\xi = (\Delta x)^{-1} \cdot \ln \frac{\Theta_\ell}{\Theta_r}$. $\tag{21}$

In one dimension, the heat transfer velocity is therefore bounded by

$$\mathbf{v}_{th} := \frac{\sum_\alpha c_{p,\alpha} \varrho_\alpha \mathbf{v}_\alpha + \bar{\lambda}_E \xi}{\hat{c}_p}, \tag{22}$$

which enhances the formulation for convective fluxes, (15).

In the notation of (11), integral measures of F_i^E per cell are desired. For each cell i in a regular grid, every principal direction yields an approximate value for the constant ξ based on two opposing interfaces. The maximum value over each principal direction gives the cell quantity ξ_i that enters the calculation of F_i^E. The largest convective flux per interface, cf. (12), is considered. Combined, this yields

$$F_i^E = \max_{\gamma \in \mathcal{N}_i} \left(\sum_\alpha \left| \mathbf{n}_\gamma^T \mathbf{v}_{\alpha,\gamma} \varrho_\alpha c_{p,\alpha} A_\gamma \right| \right) + \bar{\lambda}_E \xi_i. \tag{23}$$

The advantage of this CFL criterion is that it only reuses quantities that have to be calculated anyway in the transport scheme, thus requiring negligible additional computational efforts. An alternative mapping of the gradients at the cell's interfaces to its center has to be found if irregular grids are used. Likewise, the method presented here implicitly assumes that the temperature gradient is always in the direction of convection.

The size of the time-step is then finally determined by combining the transport of mass and energy along Eq. (11),

$$\Delta t = a \left(\min \left\{ \frac{S_i}{F_i}, \frac{S_i^E}{F_i^E} \right\} \right), \quad a \leq 1. \tag{24}$$

2.4. Discretization in space

The governing equations (8)–(10) are discretized in space with a cell-centered finite volume method (CCFV, [29]). This requires an approximation of the flux f through the interface γ of each cell i. Traditionally, the "Two-Point Flux Approximation" (TPFA) is employed, using information from the two neighboring cells, denoted by i and j:

$$f_\gamma = -A_\gamma \sum_\alpha \varrho_\alpha \mathbf{n}_\gamma^T \mathbf{v}_\alpha = -A_\gamma \mathbf{n}_\gamma^T \mathbf{K}_\gamma \mathbf{d}_{ij} \sum_\alpha \varrho_\alpha \lambda_\alpha \left(\frac{p_{\alpha,j} - p_{\alpha,i}}{\Delta x} - \varrho_\alpha \mathbf{g}^T \mathbf{d}_{ij} \right). \tag{25}$$

Here, $\mathbf{x}_i$ is the position vector of the center of cell i and $\Delta x = |\mathbf{x}_j - \mathbf{x}_i|$ is the distance to the neighboring cell j; the vector $\mathbf{d}_{ij} = (\mathbf{x}_j - \mathbf{x}_i)/\Delta x$ connects these centers scaled by the unit length. Moreover, $\mathbf{K}_\gamma$ denotes an appropriately averaged permeability at the interface γ. Although the TPFA is very robust, there are limits to its applicability, for example in the case of anisotropic permeability [30,31]. If a regular grid is locally refined and closure is omitted, which is done in our study, the TPFA fails to reproduce fluxes correctly around the hanging nodes [32].

ARTICLE IN PRESS

B. Faigle et al. / Comput. Methods Appl. Mech. Engrg. ▮ (▮▮▮▮) ▮▮▮–▮▮▮ 7

Several approaches exist that overcome these shortcomings, e.g. [10,32,33]. In this work, the stencil for the gradients on irregular faces is extended using a "multi-point flux approximation" (MPFA L-method, for details and derivation see [34]). In order to derive formulae that are valid for both approaches, TPFA and MPFA, Eq. (25) is transformed into a common form for both methods.

The index set I_γ is introduced containing all cells k that contribute to the flux stencil for the interface γ. Eq. (25) is generalized to

$$f_\gamma = -\sum_\alpha \varrho_\alpha \lambda_\alpha \sum_{k \in I_\gamma} \tau_k (p_{\alpha,k} - \varrho_\alpha \mathbf{g}^T \mathbf{x}_k). \tag{26}$$

In (26), the geometry and rock properties are combined to the "transmissivity coefficients" τ_k. Compared to the TPFA ($|I_\gamma| = 2$), the MPFA computes τ_k by solving a local problem that includes cells in the surroundings of the interface of interest, i.e. $|I_\gamma| > 2$ in general. As this is a costly operation, it is only performed where necessary, around the hanging nodes caused by grid adaptivity. If both neighboring cells lie on the same grid level, the faster TPFA is used.

The transport equation calculates the change in mass ΔC_i^κ over the next time-step for each cell i of volume V_i as

$$\frac{\Delta C_i^\kappa}{\Delta t} = \sum_\gamma \frac{A_\gamma}{V_i} \sum_\alpha \varrho_\alpha \lambda_\alpha \sum_k \tau_k \left(p_{\alpha,k} - \varrho_\alpha \mathbf{g}^T \mathbf{x}_k \right) X_\alpha^\kappa - q_i^\kappa. \tag{27}$$

The energy transport is formulated analogously as

$$\frac{\Delta \hat{u}_i}{\Delta t} = \sum_\gamma \frac{A_\gamma}{V_i} \left[\sum_\alpha \varrho_\alpha \lambda_\alpha \sum_k \tau_k \left(p_{\alpha,k} - \varrho_\alpha \mathbf{g}^T \mathbf{x}_k \right) h_\alpha - \mathbf{n}_\gamma^T \mathbf{d}_{ij} \bar{\lambda}_E \frac{T_j - T_i}{\Delta x} \right] - q_i^E. \tag{28}$$

The discretization of the pressure equation is more involved because of the derivatives in the fluid volume, which can only be assumed to be piecewise constant in each cell if slightly compressible systems are considered [10]. For other cases, a volume integral appears. To calculate it, Fritz et al. [1] propose subdividing each discrete cell i into one sub-volume per interface γ that is scaled by the face area A_γ and the cell's surface area $U_i = \sum_\gamma A_\gamma$. The volume integral over the gradient in volume derivatives is then calculated by a summation of these sub-volumes $\sum_\gamma \frac{A_\gamma}{U_i} \cdot V_i$. In each of these sub-volumes, the gradient of each volume derivative is approximated linearly between the discrete values in cell i and j, and the remaining flux expressions in the volume integral equal those in the boundary integral.

This gives the discretized pressure equation for compositional non-isothermal flow,

$$
\begin{aligned}
V_i c_{t,i} & \frac{p_i^t - p_i^{t-\Delta t}}{\Delta t} \\
& - \sum_{\gamma_{ij}} A_{\gamma_{ij}} \left[\sum_\alpha \varrho_\alpha \lambda_\alpha \sum_k \tau_k \left(p_{\alpha,k} - \varrho_\alpha \mathbf{g}^T \mathbf{x}_k \right) \left(\sum_\kappa X_\alpha^\kappa \frac{\partial \hat{v}}{\partial C^\kappa} + h_\alpha \frac{\partial \hat{v}}{\partial \hat{u}} \right) \right. \\
& \left. - \mathbf{n}_\gamma^T \mathbf{d}_{ij} \bar{\lambda}_E \frac{T_j - T_i}{\Delta x} \frac{\partial \hat{v}}{\partial \hat{u}} \right] \\
& + \sum_{\gamma_{ij}} V_i \frac{A_{\gamma_{ij}}}{U_i} \left[\sum_\alpha \varrho_\alpha \lambda_\alpha \sum_k \tau_k \left(p_{\alpha,k} - \varrho_\alpha \mathbf{g}^T \mathbf{x}_k \right) \right. \\
& \times \left(\sum_\kappa X_\alpha^\kappa \frac{\frac{\partial \hat{v}_j}{\partial C_j^\kappa} - \frac{\partial \hat{v}_i}{\partial C_i^\kappa}}{\Delta x} + h_\alpha \frac{\frac{\partial \hat{v}_j}{\partial \hat{u}_j} - \frac{\partial \hat{v}_i}{\partial \hat{u}_i}}{\Delta x} \right) - \mathbf{n}_\gamma^T \mathbf{d}_{ij} \bar{\lambda}_E \frac{T_j - T_i}{\Delta x} \frac{\frac{\partial \hat{v}_j}{\partial \hat{u}_j} - \frac{\partial \hat{v}_i}{\partial \hat{u}_i}}{\Delta x} \right] \\
& = V_i \sum_\kappa \frac{\partial \hat{v}}{\partial C^\kappa} q_i^\kappa + V_i \frac{\partial \hat{v}}{\partial \hat{u}} q_i^E + V_i \alpha_r \frac{\hat{v} - \phi}{\Delta t}.
\end{aligned}
\tag{29}
$$

The derivatives of fluid volume are computed numerically using a secant method. Its increment, meaning the expected changes in mass or energy inside each cell, is determined by a prediction step using the pressure field of the old

ARTICLE IN PRESS

8   *B. Faigle et al. / Comput. Methods Appl. Mech. Engrg. ▮ (▮▮▮▮) ▮▮▮–▮▮▮*

time-step $t - \Delta t$. This estimate also determines the upwind direction in the pressure equation. For both the pressure and the transport equation, first-order upwinding is employed.

As this formulation requires all phase pressures, and only one pressure is a primary variable, the other phase pressure is determined by the capillary pressure of the last time-step. So, if p_n is chosen to be the primary variable, the corresponding phase pressure of the wetting phase p_w is related via $p_w^t = p_n^t - p_c^{t-\Delta t}$, which induces a "capillary flux" driven by $\dots \sum_k \tau_k p_{c,k}$. The pressure field at time t is calculated with the secondary variables at time $t - \Delta t$. Hence, the volume balance in (5) is not necessarily fulfilled, and a residual,

$$\epsilon = \phi - \hat{v}, \tag{30}$$

remains. An iterative solution is avoided for reasons of efficiency. To prevent the volume error ϵ from building up, the error of the last time-step is introduced as an artificial source- or sink-term in the pressure calculation of the following time-step (last term of Eq. (29)). The error is dampened by a heuristic factor α_r, mostly in the range $0.2 \leq \alpha_r \leq 0.7$ [10]. This term can be crucial for the stability of the method, as it strongly depends on the size of the time-step. In this study, high flow velocities lead to very small but also very stable time-step sizes, which also keep the volumetric discrepancy low.

2.5. Isoenergetic and isobaric flash calculation

Isoenergetic and isobaric flash calculations performed in porous media simulations compute the composition X_α^κ, phase distribution S_α and temperature T for a given pressure, feed fraction ($Z^\kappa = C^\kappa / (\sum_\kappa C^\kappa)$) and energy. If the temperature was known, a classical isothermal isobaric flash calculation could be performed (see, e.g., [35]): given temperature, pressure and composition, the equilibrium factors K^κ are calculated using an appropriate thermodynamic model. The RACHFORD–RICE equation for two phases,

$$\sum_\kappa \frac{Z^\kappa (K_\alpha^\kappa - 1)}{1 + v_\beta (K_\alpha^\kappa - 1)} = 0, \tag{31}$$

can then be solved to get the phase fraction v_α, and thus also the saturation by means of the density,

$$S_\alpha = \frac{v_\alpha / \varrho_\alpha}{\sum\limits_\alpha (v_\alpha / \varrho_\alpha)}. \tag{32}$$

In the non-isothermal case, however, the temperature is unknown and only an internal energy u_{given} is provided. We follow the approach by Agarwal et al. [36], depicted in Fig. 3. A p, T-flash at an intermediate temperature, as discussed above, is nested in an outer loop to calculate a temperature that matches the specified energy u_{given}. An objective function is defined that relates the internal energy u_m at iteration step m to the specified internal energy from the transport solution,

$$g_{E,m} = u_m - u_{\text{given}} = \left(\left(\sum_\kappa C^\kappa \right) \sum_\alpha u_\alpha v_\alpha + (1 - \phi) \varrho_s c_s T_m \right) - u_{\text{given}}. \tag{33}$$

To avoid computing costly derivatives of thermodynamic functions, a secant method is applied to update the temperature and minimize the residual (33), yielding

$$T_{m+1} = T_m - g_{E,m} \frac{T_m - T_{m-1}}{g_{E,m} - g_{E,m-1}}. \tag{34}$$

If the fluid system remains far away from the boiling temperature, the iteration can be started with an arbitrary initialization point such as $T_{m-1} = T^{t-\Delta t} - 10\,°C$ and the temperature of the last time-step $T_m = T^{t-\Delta t}$. The according internal energies u_{m-1} and u_m are determined by a p, T-flash at those temperatures. The newly found temperature enters the regular p, T-flash, which yields the necessary quantities ϱ_α, v_α, S_α and hence also the new capillary pressure p_c to update the internal energy and determine the new residual g_E. Iteration is stopped as soon as the fraction g_E / u_{given} lies below a given tolerance.

ARTICLE IN PRESS

B. Faigle et al. / Comput. Methods Appl. Mech. Engrg. ▮ (▮▮▮▮) ▮▮▮–▮▮▮　9
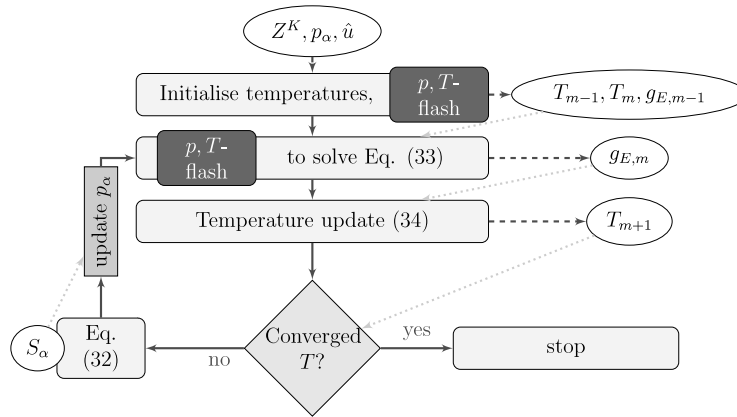
Fig. 3. NI flash for non-boiling fluids "p" abbreviates phase, "c" abbreviates component.

3. Multi-physics

In many subsurface applications, simulations are performed to estimate the effect of a local activity on the far-field: if a second fluid is injected in a well, for example, what are the effects on background flow in the reservoir, and to what extent will there be a significant increase in pressure? Can injected CO_2 displace formation brine into freshwater aquifers? In these situations, large parts of the modeling domain remain saturated by the reservoir fluid. Only in a small region of great interest, around the injection well and the plume of the injected fluid, complex physics prevail, which requires a complex model such as the one described in Section 2.

Using such involved models for simpler systems exhibits excess computational work. Multi-physics models seek to apply the least complex model locally that still captures the relevant processes to assemble the global solution system efficiently. To do so, the modeling domain is divided into non-overlapping sub-domains with different model complexity. In this work, a two-phase sub-domain distinguishes between cells where a single- or a two-phase model is applied (as is done in [2,1]), and a further NI-sub-domain indicates where the full non-isothermal functionality is employed.

Faigle et al. [2] show for isothermal systems that the pressure equation can be simplified significantly for single-phase situations: the phase compressibility c_α rather than $\hat{c}$ is sufficient; the derivative in the fluid volume then equals the phase density, and its gradients (the term over lines 4 and 5 of Eq. (29)) vanish,

$$V_i c_\alpha \frac{p_i^t - p_i^{t-\Delta t}}{\Delta t} + \sum_{\gamma_{ij}} A_{\gamma_{ij}} \lambda_\alpha \sum_k \tau_k \left(p_{\alpha,k} - \varrho_\alpha \mathbf{g}^T \mathbf{x}_k \right) = V_i \frac{\sum_\kappa q_i^\kappa}{\varrho_\alpha} + V_i \alpha_r \frac{v_\alpha - \phi}{\Delta t}. \tag{35}$$

Under non-isothermal conditions, the fluid volume can change drastically in single-phase regions as well. Hence, the volume derivatives and their gradients cannot be fully neglected. The pressure equation can nevertheless be simplified to

$$V_i c_\alpha \frac{p_{\alpha,i}^t - p_{\alpha,i}^{t-\Delta t}}{\Delta t} - \sum_{\gamma_{ij}} A_{\gamma_{ij}} \left[\lambda_\alpha \sum_k \tau_k \left(p_{\alpha,k} - \varrho_\alpha \mathbf{g}^T \mathbf{x}_k \right) \left(1 + \varrho_\alpha h_\alpha \frac{\partial v_\alpha}{\partial u_\alpha} \right) + \mathbf{d}_{ij} \bar{\lambda}_E \frac{T_j - T_i}{\Delta x} \frac{\partial v_\alpha}{\partial u_\alpha} \right]$$

$$+ \sum_{\gamma_{ij}} V_i \frac{A_{\gamma_{ij}}}{U_i} \left[h_\alpha \lambda_\alpha \sum_k \tau_k \left(p_{\alpha,k} - \varrho_\alpha \mathbf{g}^T \mathbf{x}_k \right) + \mathbf{d}_{ij} \bar{\lambda}_E \frac{T_j - T_i}{\Delta x} \frac{\partial v_\alpha}{\partial u_\alpha} \right] \frac{\frac{\partial v_{\alpha,j}}{\partial u_\alpha} - \frac{\partial v_{\alpha,i}}{\partial u_\alpha}}{\Delta x}$$

$$= V_i \frac{\sum_\kappa q_i^\kappa}{\varrho_\alpha} + V_i \alpha_r \frac{v_\alpha - \phi}{\Delta t}. \tag{36}$$

In principle, the temperature in simulations with the non-isothermal model is the result of the iterative u, p-flash (Section 2.5). A linear approximation of the temperature is sufficient if the system is single-phase and changes in

ARTICLE IN PRESS

10   B. Faigle et al. / Comput. Methods Appl. Mech. Engrg. ▮ (▮▮▮▮) ▮▮▮–▮▮▮

Table 1
Multi-physics summary.

Sub-domain	Pressure equation	Volume derivatives	Flash
1p2c	Eq. (35)	No	No
1p2c-NI	Eq. (36)	$\partial v_w / \partial u_w$ with Δv_w via new T from (37)	u, p-flash
2p2c	Eq. (21) in [2]	All but $\partial \hat{v} / \partial \hat{u}$	p, T-flash, T via (37)
2p2c-NI	Eq. (29)	All	u, p-flash
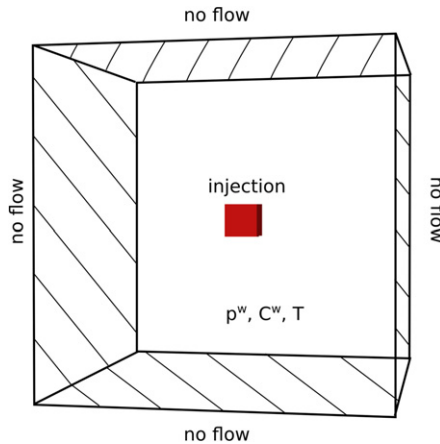
Fig. 4. Simulation domain and boundary conditions. Red cuboid marks the injection area.

temperature are marginal,

$$T = T_{\text{init}} + \frac{1}{\hat{c}_v} \left(\hat{u} - \hat{u}(T_{\text{init}}) \right), \tag{37}$$

$$\hat{c}_v = (1 - \phi) \varrho_s c_s + \phi \varrho_\alpha c_{v,\alpha}. \tag{38}$$

Outside the NI-sub-domain, (37) provides a temperature that is directly used in a p, T-flash to obtain the secondary variables. This linear approximation can also provide an approximation for the estimated change in temperature, which allows a direct calculation of volume derivatives in (36) by means of one additional p, T-flash with $T + (\Delta T)_{\text{est}}$.

Table 1 summarizes the four different levels of model complexity that are incorporated in our multi-physics approach. The assignment of a cell to one of the sub-domains is updated in each time step. By respectively adding one element layer around the NI-sub-domain and the 2p2c-sub-domain, the CFL condition guarantees that those sub-domains are large enough such that the model complexity associated with one cell will not increase during one time step. For more details on the selection of the sub-domains, we refer to the isothermal case treated in [2,1].

4. Numerical examples

The numerical model described in the previous sections has been implemented in the open-source porous-media simulator DuMu^x [37], which is based on the Distributed and Unified Numerics Environment DUNE [38]. As grid manager, ALUGrid is employed [39], which provides the necessary capabilities for local grid adaptivity. The model will be tested by means of two numerical examples. In Section 4.1, a simple problem setup is chosen to analyze the efficiency gain for using the multi-physics model compared to the full model and to investigate the influence of the injection rate on the size of the sub-domains. Section 4.2 is devoted to a more demanding problem setup that involves parameters taken from a real reservoir.

ARTICLE IN PRESS

B. Faigle et al. / Comput. Methods Appl. Mech. Engrg. ▌ (▌▌▌▌) ▌▌▌–▌▌▌   11
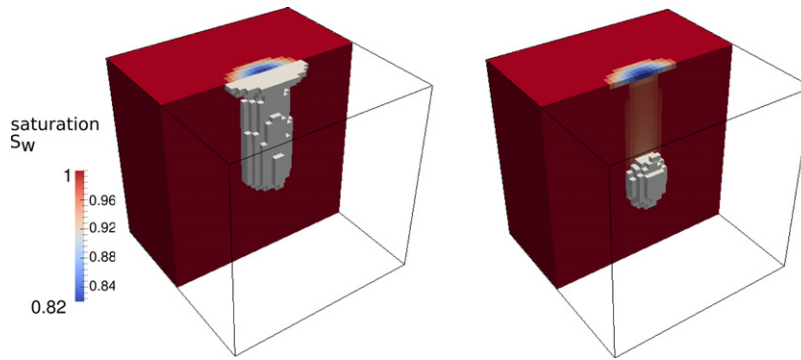
Fig. 5. 2-phase sub-domain (left) and non-isothermal sub-domain (right) in one half of the domain (white color). Saturation distribution is shown in the other half of the domain.
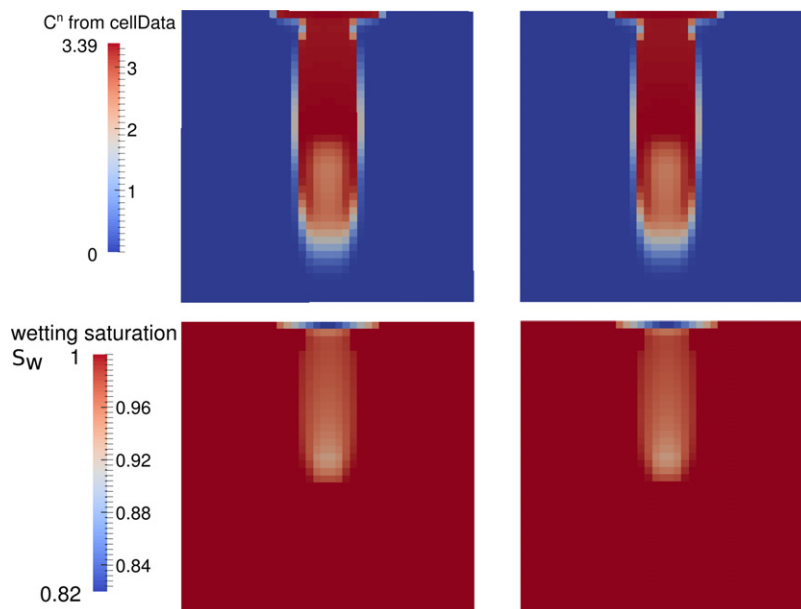

Fig. 6. Vertical slice through the center of the domain. Total concentration of CO_2 (top row) and plume extent (bottom row) after 42 h for the full non-isothermal compositional two-phase model (left column) and the multi-physics model (right column).

4.1. Efficiency analysis and influence of the injection rate

A three-dimensional simulation domain has been chosen to compare the multi-physics model with a full non-isothermal compositional two-phase model in terms of computational efficiency. The bottom and top as well as two opposing sides of the domain are confined by no-flow boundaries, with constant pressure conditions on the remaining side boundaries at 1 MPa (see Fig. 4). The domain is a cuboid with equal side lengths of 10 m. CO_2 at 423.15 K is injected in the middle of the domain in a cuboid with equal side lengths of 1 m at an injection rate of 117 kg/h. The domain is initially saturated with brine at 288.15 K. To analyze the efficiency of the multi-physics algorithm the simulation is run on a non-adaptive grid with $40 \times 40 \times 40$ cells (64,000 cells in total). Table 2 lists the soil parameters and Table 3 lists the parameters used in the simulation.

The multi-physics model and the full non-isothermal compositional two-phase model show perfectly agreeing results (Fig. 6). During the simulation time of 42 h the CO_2 phase rises fast to the top of the domain where it accumulates and starts to spread. Some of the CO_2 dissolves in brine and slowly moves towards the bottom of the domain. Results from the multi-physics model (Fig. 5) show that the two-phase sub-domain tracks the evolution of the CO_2 plume, that means the part of the domain where two phases are present. The non-isothermal sub-domain evolves

ARTICLE IN PRESS

12   *B. Faigle et al. / Comput. Methods Appl. Mech. Engrg.* ▮ *(▮▮▮▮)* ▮▮▮–▮▮▮
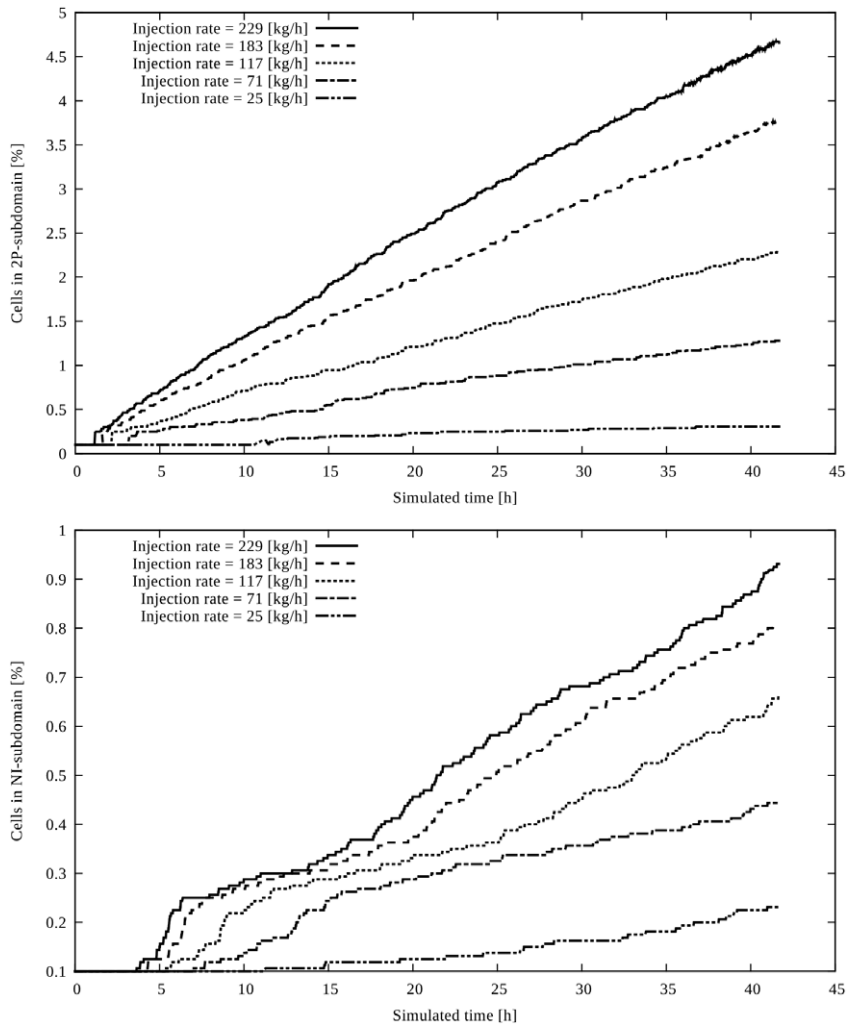
Fig. 7. Percentage of cells in 2-phase (top) and non-isothermal sub-domain (bottom) with varying injection rate.

Table 2
Soil parameters for the efficiency analysis.

Porosity ϕ	Permeability K	Thermal conductivity λ_s
0.005	$1e-11$ m^2	2 W/(m K)

Table 3
Simulation parameters for the efficiency analysis.

Residual saturations		BC-parameter		CFL	Error
$S_{w,r}$	$S_{n,r}$	p_d	λ	factor a	factor a_e
0.1	0.0	10,000 Pa	2	0.7	0.7

near the injection area of CO_2, and partly spreads downwards. Near the injection area the non-isothermal sub-domain is overlapping with the two-phase sub-domain. Full non-isothermal two-phase effects are considered here. Full non-

ARTICLE IN PRESS

B. Faigle et al. / Comput. Methods Appl. Mech. Engrg. ▮ (▮▮▮▮) ▮▮▮–▮▮▮   13
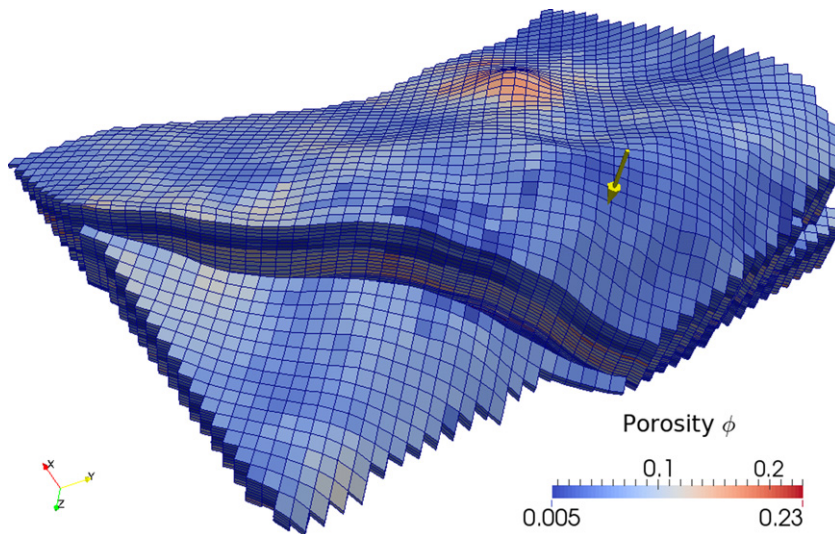
Fig. 8. Porosity distribution in the Tensleep formation. The vertical model dimension is scaled by a factor four. The yellow arrow marks the injection well.

isothermal effects under single-phase conditions are modeled below the injection area. In this part of the domain flow processes are slower, resulting in less convection and thus a higher change in temperature due to the CO_2 injection.

The multi-physics model considers two-phase effects during the whole simulation time for this specific problem only for a maximum of 2.2 % of the cells. Full non-isothermal effects are only considered for a maximum of 0.6 % of the cells. As a result, the multi-physics model requires only 20 % of the CPU time that is needed for the full non-isothermal compositional two-phase model. For this simple problem setup, this shows the efficiency gain due to the multi-physics framework which allows the solution of a simpler and computationally less demanding model abstraction in most parts of the domain without losing accuracy of the solution.

Similar simulations are carried out to determine how the relation of advection to diffusion influences the evolution of the multi-physics sub-domains. For this purpose the injection rate of CO_2 is varied between 25, 71, 117, 183 and 229 kg/h to enhance advection in the system by a larger influx of CO_2. The same simulation setup and parameters as above are chosen. The percentage of cells belonging to the sub-domains are shown in Fig. 7. An increase of the injection rate leads to an increase in the size of the plume and thus to a larger two-phase sub-domain. The size of the non-isothermal sub-domain depends on the number of cells where the temperature compared to the initial temperature exceeds a certain value. The non-isothermal sub-domain increases with a larger injection rate because along with the mass injected also the energy in the system increases.

4.2. Modeling of the Tensleep formation

In the following, the multi-physics model is applied to a realistic field test case. The background is described in Section 4.2.1, while the problem setup is presented in Section 4.2.2. Section 4.2.3 is devoted to the numerical challenges that result from this complex setup, and Section 4.2.4 finally presents the simulation results.

4.2.1. Background

A large-scale example of a real subsurface reservoir has been selected to show the applicability of the concepts presented in this work to a very challenging physical problem. We use a model of the Tensleep formation [40,41] in Wyoming, USA. This formation comprises mainly clastic sediments (sandstones) as well as some dolomites. It contains the only federally owned and operated oil field in the USA and has the advantage that the reservoir data are in the public domain. In the course of field operation, strategies such as gas injection were introduced in the field for enhanced oil recovery purposes. For simplicity, we assume that all accessible flow paths are already fully filled with brine, because water has been produced for decades [42].

ARTICLE IN PRESS

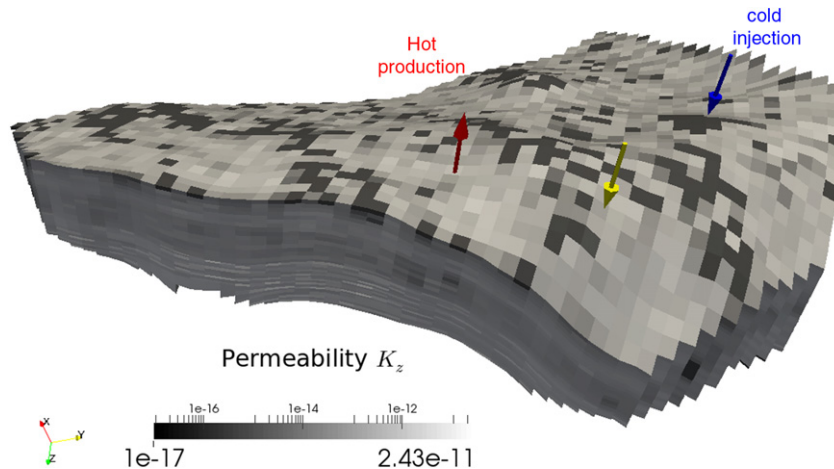14   B. Faigle et al. / Comput. Methods Appl. Mech. Engrg. ∎ (∎∎∎∎) ∎∎∎–∎∎∎

Fig. 9. Simulation domain for adaptive simulations without degenerated elements (i.e. only the cells of the main reservoir region bounded by the sealing fault), showing the vertical permeability K_z in (m^2). The vertical model dimension is scaled by a factor four. (For interpretation of the references to color in this figure legend, the reader is referred to the web version of this article.)

Due to its dome-shaped structure (Fig. 8), being one interval within the "teapot dome" oil field, and the availability of detailed data, this formation is perfectly suited for scientific studies on CO_2 injection. The outer regions of the Tensleep formation are also being considered for geothermal energy extraction. Possibly, CO_2 storage and geothermal energy extraction can be combined (e.g. Randolph et al. [43], Salimi and Wolf [44], Buscheck et al. [45]), but this requires re-injection of the produced cold brine.

After decades of production, the Tensleep formation still remains at approximately 88 °C and a multitude of wells are available as well. Thus, a concurrent geothermal usage of extracted formation fluid may be possible in principle. Such a scenario provides an excellent opportunity to apply the concepts presented in this work to a real-world subsurface problem: using the Tensleep formation for concurrent CO_2 storage and geothermal extraction requires a numerical framework that can handle the complex physical processes pertinent to both applications. Considering the large simulation domain, both types of physical complexity occur in only restricted model sub-regions. Hence, this modeling problem is well-suited for the multi-physics framework. In particular, the initial grid resolution of 30 m × 30 m needs to be refined to properly resolve the flow between the wells, which are spaced approximately 450 m apart.

This section shows a simulation using the multi-physics framework with adaptive grid refinement for a real reservoir under challenging operating conditions, highlighting its advantages and weaknesses. This proof-of-concept study is intended neither to investigate the feasibility of such an operation nor to evaluate the injection strategy.

4.2.2. Description of the formation and simulation setup

The full simulation domain is depicted in Fig. 8, featuring a dome-shaped structure that is intersected by a large sealing fault. The simulation grid follows the geological model, which was set up using seismic data and data from 15 well logs. Porosity and permeability distributions in the field were modeled using geostatistic methods that were conditioned to the well data. In addition, the original geological model contained a stochastically generated discrete fracture network, which was set up using well and outcrop data [46]. Although such a fractured reservoir should be modeled using a dual-continua formulation, this is beyond the scope of this study. As the matrix permeability is very low and the fracture network highly connected, we use the fracture permeability and the matrix porosity, fully acknowledging that the exchange processes between the fracture and matrix are not properly modeled.

The bottom and top of the domain are confined by a no-flow boundary, with hydrostatic pressure conditions on the side boundaries at 2370 psi (≈16 MPa) on the reference level of 60 m below sea level [47]. Well "44-1-TpX-10" is the injection well. It is assumed that 104 tons/day of CO_2 [47] are injected at 35 °C into the sandstone layer which has the highest storage capacity. For coupled geothermal usage (see Fig. 9), brine is injected at 40 °C into well "56-TpX" (blue arrow). Hot reservoir fluids are produced from well "54-TpX" (red arrow). The available grid managers that provide grid adaptivity are not able to manage the non-conforming cell interfaces along faults. In order to apply grid refinement, all cells behind the faults have been excluded from the simulation. Only the main reservoir area where

ARTICLE IN PRESS

B. Faigle et al. / Comput. Methods Appl. Mech. Engrg. ▮ (▮▮▮▮) ▮▮▮–▮▮▮   15

Table 4
Simulation parameters for the Tensleep formation.

Residual saturations		BC-parameter		CFL	Error
$S_{w,r}$	$S_{n,r}$	p_d	λ	factor a	factor a_e
0.1	0.1	2000 Pa	2	0.7	0.3
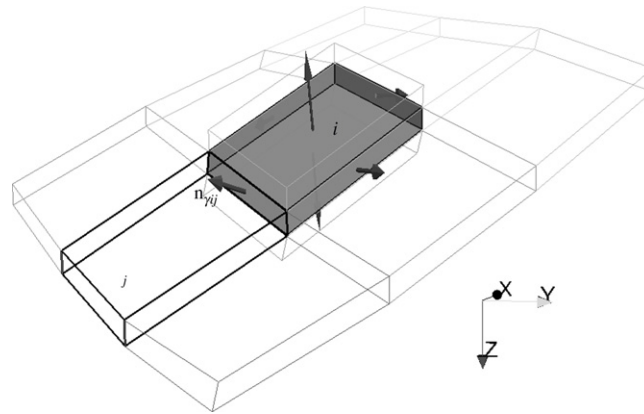
Fig. 10. Twisted faces may lead to skewed face normals and require a modified flux term.

the wells are located remains in the simulation domain (Fig. 9) if an adaptive grid is used. Chiaramonte et al. [48] consider the main fault in the Tensleep formation to be sealing, so this is not an unreasonable simplification of the model domain. Table 4 lists the parameters used in the simulation.

The multi-physics framework employed in our study considers four different levels of complexity; all include compositional and compressible effects (Table 1):

- A full non-isothermal two-phase region evolves near the CO_2 injection well. This is the most complex model and is also applied in all cells containing wells.
- A two-phase model with a linear approximation of temperature is applied in regions where the CO_2 plume has already reached reservoir temperature.
- Full non-isothermal effects under single-phase conditions are modeled near the cold brine injection well, and below the CO_2 injection well where gravitational forces prevent the CO_2 phase from reaching deeper parts of the reservoir, but where the reservoir temperature has been altered by the injection.
- A single-phase model with a linear approximation of the temperature is applied in the far-field region of the reservoir.

4.2.3. Numerical challenges for simulating the field

The flux expressions (25) require some modification to avoid errors in the flux calculations with the TPFA. There are strongly deformed ("twisted") cell faces in the field, see Fig. 10, which arise due to the combined constraints on the geometrical dome structure and the underlying rock properties. The gray cell i resides above the black-edged cell j, thus the vector connecting the cell's centers $\mathbf{d}_{ij}$ points downwards. The figure also depicts the normals $\mathbf{n}_{\gamma_i}$ on the center points of all interfaces γ_i. In the case of the interface γ_{ij} between the gray and black-edged cell, $\mathbf{n}_{\gamma_{ij}}$ points upwards because this interface γ_{ij} is strongly twisted. In this case, $\mathbf{n}_\gamma^T \mathbf{d}_{ij}$ becomes negative, and (25) would yield a flux in the wrong direction. To avoid this mistake, the absolute value of the term $|\mathbf{n}_\gamma^T \mathbf{K} \mathbf{d}_{ij}|$ is used to calculate the fluxes. Such "corrections" would not be necessary if the MPFA method was employed on all cell faces, so this deficiency arises because of the combination of MPFA and TPFA in this study.

Any coarsening or refinement of a grid cell is triggered by appropriate indicators. In [2], refinement at the injection front is realized by an indicator based on the differences in phase saturation. In this study, differences in temperature act as an additional indicator to refine thermal fronts as well. If only these two indicators are combined, a non-physical pressure field is eventually computed on an adaptive grid, even if a direct solver is employed (Fig. 11(a)). An
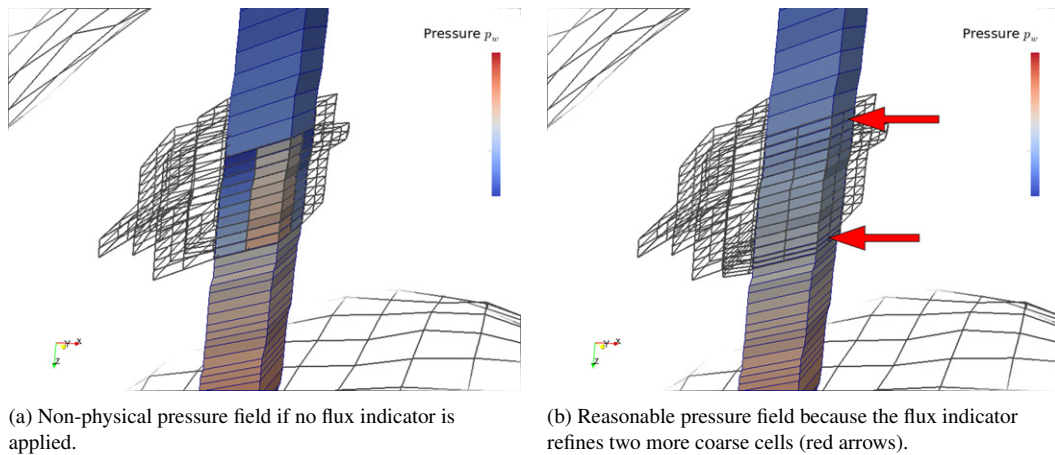
ARTICLE IN PRESS

16   *B. Faigle et al. / Comput. Methods Appl. Mech. Engrg.* ▮ *(▮▮▮▮)* ▮▮▮–▮▮▮

(a) Non-physical pressure field if no flux indicator is applied.

(b) Reasonable pressure field because the flux indicator refines two more coarse cells (red arrows).

Fig. 11. Grid and a pile of cells cut out near the CO_2 injection well.
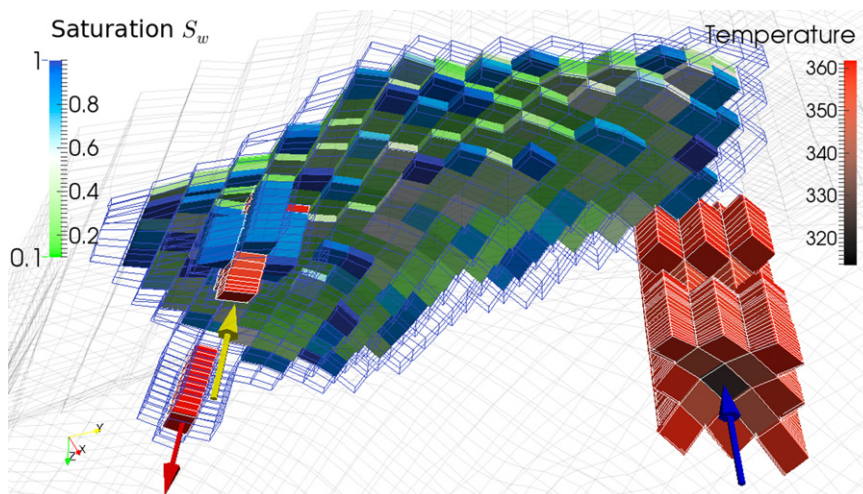
Fig. 12. Simulation after 290 days of CO_2 injection (yellow arrow) and geothermal production (red arrow) with cold injection (blue arrow) seen from below the formation. The cells of the NI-sub-domain are cornered white, those of the two-phase sub-domain blue. (For interpretation of the references to color in this figure legend, the reader is referred to the web version of this article.)

additional flux indicator is hence added that investigates the fluxes F_i calculated for the CFL-criterion (12) and refines cells where large fluxes are observed. To prevent oscillating refinement and coarsening, each cell that became refined by the flux indicator can only be coarsened again if four consecutive adaptation steps do not call for a refinement. In this way, non-physical pressure fields and the subsequent termination of the simulation can be avoided (Fig. 11(b)).

4.2.4. Simulation results

Preliminary runs on the full coarse domain show that the injected CO_2 rises rapidly through the fracture network and accumulates below the cap-rock (see also [47]). The plume spreads above the target interval whose large porosity would provide the desired storage capacity.

Within one year of injection, the cold CO_2 does not lead to a substantial decrease in temperature in the vicinity of the CO_2 well. Hence, the major part of the plume can be modeled with simpler and faster model complexity. The injection of cold water, however, reduces the formation temperature gradually, leading to a zone of significant temperature differences around the brine injection well.

ARTICLE IN PRESS

B. Faigle et al. / Comput. Methods Appl. Mech. Engrg. ▮ (▮▮▮▮) ▮▮▮–▮▮▮

17
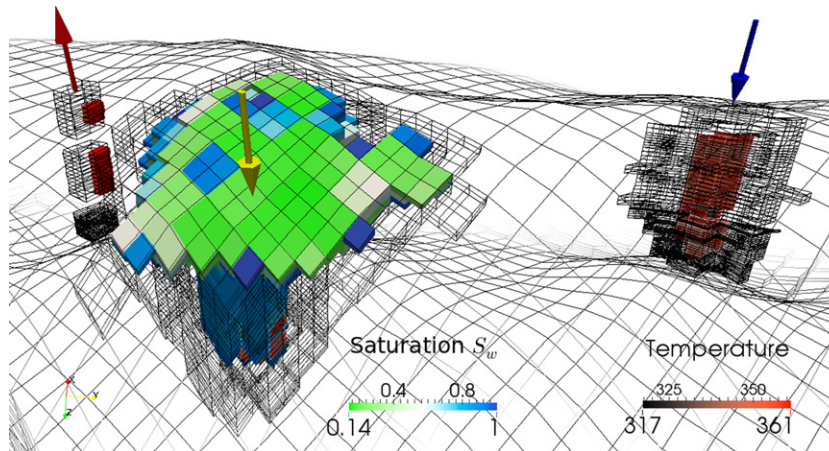
(a) View from above the formation.

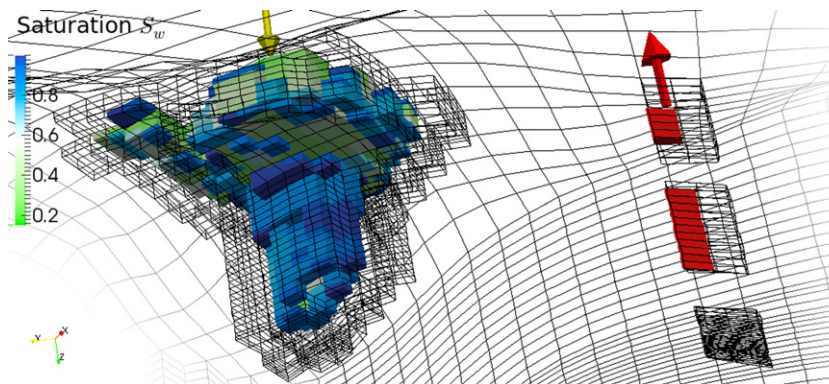(b) View on the red extraction and yellow CO_2 injection well.

Fig. 13. CO_2 plume and NI-sub-domain (red cells) after $2 \cdot 10^6$ s ($\approx$24 days). (For interpretation of the references to color in this figure legend, the reader is referred to the web version of this article.)

After 290 days, this zone begins to interact with the CO_2 plume (Fig. 12). The CO_2 rises rapidly upwards and then spreads above the desired storage formation, while the temperature changes induced by the brine injection are observable in this layer as well. In that period, the injection of 60 ktons of brine and the production of 75 ktons of hot brine (and 57 tons of CO_2) could not yet significantly affect the subsurface behavior of the injected 30 ktons of CO_2.

The simulation results for an adaptively refined grid are shown in Figs. 13 and 14. All single-phase cells modeled with a linear temperature approximation are removed to show the grid. Fig. 13(b) provides a more detailed view of the CO_2 injection area. The detailed flow paths of the CO_2 start to become visible. Below the extraction well, some cells are refined by the flow indicator, which is required for stability reasons (Section 4.2.3). In this area, however, strong non-linearities in the pressure field and thus potentially non-monotone pressure solutions are not expected. This refinement therefore does not necessarily improve the stability of the pressure solve. On the contrary, due to their small grid size in the vertical direction, these refined cells influence the size of the time-step negatively. Here, a further development of the flux indicator would be beneficial to generate just enough refinement to prevent simulation failure.

The CO_2 front already approaches the domain boundary in the refined simulations after approximately 210 days (Fig. 14). At this time, the full non-isothermal model is only required in 4% of all simulation cells. The two-phase sub-domain only covers 16% of all cells, which means that the vast majority of the global domain is efficiently solved by a simpler and computationally more efficient model abstraction.
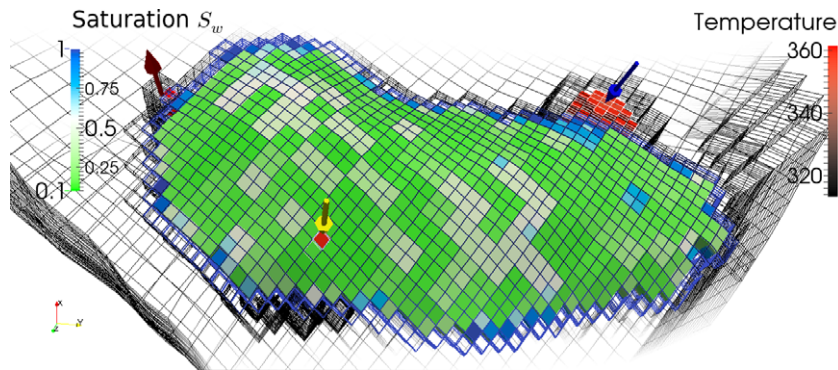
ARTICLE IN PRESS

18   *B. Faigle et al. / Comput. Methods Appl. Mech. Engrg.* ▮ *(▮▮▮▮) ▮▮▮–▮▮▮*

Fig. 14. CO_2 plume extend and grid after 200 days.

5. Conclusions

This work combines two adaptive modeling strategies for compositional two-phase flow in porous media including non-isothermal effects: a multi-physics concept selects different numerical models locally depending on the physical processes at hand; an adaptive modification of the simulation grid is used to track features of interest locally with a refined grid while allowing a coarser mesh globally. For the latter, a multi-point flux approximation (MPFA) avoids errors in the flux representation around the hanging nodes that evolve through refinement. A large-scale example related to CO_2 sequestration combined with geothermal application illustrates the potential and applicability of the presented framework.

References

[1] J. Fritz, B. Flemisch, R. Helmig, Decoupled and multiphysics models for non-isothermal compositional two-phase flow in porous media, Int. J. Numer. Anal. Model. 9 (1) (2012) 17–28.

[2] B. Faigle, R. Helmig, I. Aavatsmark, B. Flemisch, Efficient multiphysics modelling with adaptive grid refinement using a MPFA method, Comput. Geosci. (2014) 1–12.

[3] G. Ács, S. Doleschall, E. Farkas, General purpose compositional model, Soc. Pet. Eng. J. (1985) 543–553.

[4] M. Peszyńska, Q. Lu, M.F. Wheeler, Multiphysics coupling of codes, in: Computational Methods in Water Resources, 2000, pp. 175–182.

[5] M. Peszyńska, Multiphysics coupling of three-phase and two-phase models of flow in porous media, in: W. Wendland, M. Efendiev (Eds.), in: Lecture Notes in Applied and Computational Mechanics, vol. 12, Springer, Berlin, Heidelberg, 2003, pp. 311–316. URL: http://dx.doi.org/10.1007/978-3-540-36527-3_37.

[6] M. Wheeler, T. Arbogast, S. Bryant, J. Eaton, Q. Lu, M. Peszynska, I. Yotov, A parallel multiblock/multidomain approach for reservoir simulation, in: SPE 51884, 1999.

[7] M.F. Wheeler, M. Peszyńska, Computational engineering and science methodologies for modeling and simulation of subsurface applications, Adv. Water Resour. 25 (2002) 1147–1173.

[8] Z. Heinemann, G. Gerken, G. von Hantelmann, Using local grid refinement in a multiple-application reservoir simulator, in: SPE Reservoir Simulation Symposium, 15–18 November 1983, San Francisco, California, 1983. http://dx.doi.org/10.2118/12255-MS.

[9] S. Mehl, M.C. Hill, Three-dimensional local grid refinement for block-centered finite-difference groundwater models using iteratively coupled shared nodes: a new method of interpolation and analysis of errors, Adv. Water Resour. 27 (2004) 899–912.

[10] G.S.H. Pau, J.B. Bell, A.S. Almgren, K.M. Fagnan, M.J. Lijewski, An adaptive mesh refinement algorithm for compressible two-phase flow in porous media, Comput. Geosci. 16 (2012) 577–592.

[11] R.C. Hornung, J.A. Trangenstein, Adaptive mesh refinement and multilevel iteration for flow in porous media, J. Comput. Phys. 136 (1997) 522–545.

[12] J.A. Trangenstein, Multi-scale iterative techniques and adaptive mesh refinement for flow in porous media, Adv. Water Resour. 25 (2002) 1175–1213.

[13] J. Nilsson, M.G. Gerritsen, R. Younis, An adaptive, high-resolution simulation for steam-injection processes, in: SPE Western Regional Meeting, Society of Petroleum Engineers, Irvine, California, 2005, http://dx.doi.org/10.2118/93881-MS. URL: http://www.onepetro.org/mslib/app/Preview.do?paperNumber=SPE-93881-MS&societyCode=SPE.

[14] G.S.H. Pau, J.B. Bell, K. Pruess, A.S. Almgren, M.J. Lijewski, K. Zhang, High resolution simulation and characterization of density-driven flow in CO_2 storage in saline aquifers, Adv. Water Resour. 33 (4) (2010) 443–455.

[15] S. Thomas, M. Wheeler, Enhanced velocity mixed finite element methods for modeling coupled flow and transport on non-matching multiblock grids, Comput. Geosci. 15 (2011) 605–625. http://dx.doi.org/10.1007/s10596-011-9227-5.

[16] V. Hauge, K.-A. Lie, J. Natvig, Flow-based coarsening for multiscale simulation of transport in porous media, Comput. Geosci. 16 (2) (2012) 391–408.

ARTICLE IN PRESS

B. Faigle et al. / Comput. Methods Appl. Mech. Engrg. ∎ (∎∎∎∎) ∎∎∎–∎∎∎ 19

[17] I. Aavatsmark, T. Barkve, O. Bøe, T. Mannseth, Discretization on non-orthogonal, curvilinear grids for multi-phase flow, in: 4th European Conference on the Mathematics of Oil Recovery, 1994.

[18] M.G. Edwards, C.F. Rogers, A flux continuous scheme for the full tensor pressure equation, in: Proceedings of 4th European Conference on the Mathematics of Oil Recovery, EAGE, Norway, 1994.

[19] I. Aavatsmark, G.T. Eigestad, B.T. Mallison, J.M. Nordbotten, A compact multipoint flux approximation method with improved robustness, Numer. Methods Partial Differential Equations 24 (2008) 1329–1360.

[20] I. Aavatsmark, G.T. Eigestad, B. ove Heimsund, B. Mallison, J.M. Nordbotten, E. ian, A new finite-volume approach to efficient discretization on challenging grids, SPE J. 09 (2010) 658–669.

[21] M. Darcis, Coupling models of different complexity for the simulation of COstorage in deep saline aquifers (Ph.D. thesis), Universität Stuttgart, 2012.

[22] J. Trangenstein, J. Bell, Mathematical structure of compositional reservoir simulation, SIAM J. Sci. Stat. Comput. (1989) 817–845.

[23] Z. Chen, Q. Guan, R. Ewing, Analysis of a compositional model for fluid flow in porous media, SIAM J. Appl. Math. 60 (2000) 747–777.

[24] D.E.A. van Odyck, J.B. Bell, F. Monmont, N. Nikiforakis, The mathematical structure of multiphase thermal models of flow in porous media, Proc. R. Soc. A: Math. Phys. Eng. Sci. 465 (2102) (2008) 523–549.

[25] J. Fritz, A decoupled model for compositional non-isothermal multiphase flow in porous media and multiphysics approaches for two-phase flow (Ph.D. thesis), Universität Stuttgart, 2010.

[26] K. Coats, Impes stability: Selection of stable timesteps, SPE J. 8 (2003) 181–187.

[27] R. Helmig, J. Niessner, B. Flemisch, M. Wolff, J. Fritz, Efficient modelling of flow and transport in porous media using multi-physics and multi-scale approaches, in: Handbook of Geomathematics, vol. 1, 2010, pp. 417–457.

[28] S. Geiger, T. Driesner, C.A. Heinrich, S.K. Matthai, Multiphase thermohaline convection in the earth's crust: I. A new finite element—finite volume solution technique combined with a new equation of state for $NaCl–H_2O$, Transp. Porous Media 63 (2006) 399–434.

[29] R. Helmig, Multiphase Flow and Transport Processes in the Subsurface, Springer Verlag, 1997.

[30] I. Aavatsmark, T. Barkve, O. Bøe, T. Mannseth, Discretization on non-orthogonal, quadrilateral grids for inhomogeneous, anisotropic media, J. Comput. Phys. 127 (1996) 2–14.

[31] H. Class, R. Helmig, J. Niessner, U. Ölmann, Multiphase processes in porous media, in: R. Helmig, A. Mielke, B. Wohlmuth (Eds.), Multifield Problems in Solid and Fluid Mechanics, in: Lecture Notes in Applied and Computational Mechanics, vol. 28, Springer, Berlin, Heidelberg, 2006, pp. 45–82. URL: http://dx.doi.org/10.1007/978-3-540-34961-7_2.

[32] M.G. Edwards, Elimination of adaptive grid interface errors in the discrete cell centered pressure equation, J. Comput. Phys. 126 (1996) 356–372.

[33] J.A. Wheeler, M.F. Wheeler, I. Yotov, Enhanced velocity mixed finite element methods for flow in multiblock domains, Comput. Geosci. 6 (2002) 315–332. Springerlink: http://dx.doi.org/10.1023/A:1021270509932.

[34] I. Aavatsmark, Multipoint flux approximation methods for quadrilateral grids, in: 9th International Forum on Reservoir Simulation, Abu Dhabi, 2007.

[35] M.L. Michelsen, J.M. Mollerup, Thermodynamic Models: Fundamentals & Computational Aspects, Tie-Line Publications, 2007.

[36] R. Agarwal, Y.-K. Li, L. Nghiem, D. Coombe, Multiphase multicomponent isenthalpic flash calculations, J. Can. Pet. Technol. 30 (1991).

[37] B. Flemisch, M. Darcis, K. Erbertseder, B. Faigle, A. Lauser, K. Mosthaf, S. Müthing, P. Nuske, A. Tatomir, M. Wolff, R. Helmig, DUMUX: DUNE for multi-{phase, component, scale, physics, . . . } flow and transport in porous media, Adv. Water Resour. 34 (2011) 1102–1112.

[38] P. Bastian, M. Blatt, A. Dedner, C. Engwer, R. Klöfkorn, R. Kornhuber, M. Ohlberger, O. Sander, A generic grid interface for parallel and adaptive scientific computing. Part II: implementation and tests in DUNE, Computing 82 (2008) 121–138.

[39] A. Burri, A. Dedner, R. Klöfkorn, M. Ohlberger, An efficient implementation of an adaptive and parallel grid in DUNE, in: E. Krause, Y. Shokin, M. Resch, N. Shokina (Eds.), Notes in Numerical Fluid Mechanics and Multidisciplinary Design, vol. 91, Springer, Berlin, Heidelberg, 2006, pp. 67–82. URL: http://dx.doi.org/10.1007/3-540-31768-6_7.

[40] A. Ouenes, T.C. Anderson, D. Klepacki, A. Bachir, D. Boukhelf, G.C. Robinson, M. Holmes, B.J. Black, V.W. Stamp, Integrated characterization and simulation of the fractured tensleep reservoir at teapot dome for CO_2 injection design, in: SPE Western Regional Meeting, Society of Petroleum Engineers, Anaheim, California, USA, 2010, http://dx.doi.org/10.2118/132404-MS. URL: http://www.onepetro.org/mslib/app/Preview.do?paperNumber=SPE-132404-MS&societyCode=SPE.

[41] C.M. Sayers, L.D. den Boer, Characterizing production-induced anisotropy of fractured reservoirs having multiple fracture sets, Geophys. Prospect. 60 (2012) 919–939.

[42] S.J. Friedmann, V.W. Stamp, Teapot dome: characterization of a CO_2-enhanced oil recovery and storage site in Eastern Wyoming, Environ. Geosci. 13 (2006) 181–199.

[43] J.B. Randolph, M.O. Saar, J. Bielicki, Geothermal energy production at geologic CO_2 sequestration sites: Impact of thermal drawdown on reservoir pressure, Energy Procedia 37 (2013) 6625–6635.

[44] H. Salimi, K.-H. Wolf, Integration of heat-energy recovery and carbon sequestration, Int. J. Greenhouse Gas Control 6 (2012) 56–68.

[45] T.A. Buscheck, T.R. Elliot, M.A. Celia, M. Chen, Y. Sun, Y. Hao, C. Lu, T.J. Wolery, R.D. Aines, Integrated geothermal-CO_2 reservoir systems: reducing carbon intensity through sustainable energy production and secure CO_2 storage, Energy Procedia 37 (2013) 6587–6594.

[46] M. Ahmed Elfeel, S. Jamal, C. Enemanna, D. Arnold, S. Geiger, Effect of DFN upscaling on history matching and prediction of naturally fractured reservoirs, in: 75th EAGE Conference & Exhibition Incorporating SPE EUROPEC, Society of Petroleum Engineers, London, United Kingdom, 2013, http://dx.doi.org/10.2118/164838-MS. URL: http://www.onepetro.org/mslib/app/Preview.do?paperNumber=SPE-164838-MS&societyCode=SPE.

[47] L. Chiaramonte, M.D. Zoback, J.S. Friedmann, V.W. Stamp, 3D stochastic reservoir model and fluid flow simulation of a CO_2-EOR pilot in a fractured reservoir, in: Carbon Management Technology Conference, Carbon Management Technology Conference, Orlando, Florida, USA, 2012, http://dx.doi.org/10.7122/151480-MS. URL: http://www.onepetro.org/mslib/app/Preview.do?paperNumber=CMTC-151480-MS&societyCode=CMTC.

[48] L. Chiaramonte, M. Zoback, J. Friedmann, V. Stamp, Seal integrity and feasibility of CO_2 sequestration in the teapot dome eor pilot: geomechanical site characterization, Environ. Geol. 54 (2008) 1667–1675.